



The primary controlling parameters of porosity, permeability, and seepage capability of tight gas reservoirs: a case study on Upper Paleozoic Formation in the eastern Ordos Basin, Northern China

Hong-Jun Qu¹ · Bo Yang¹ · Xia-He Tian¹ · Xin-She Liu² · Huan Yang¹ · Wen-Wu Dong¹ · Ya-Hui Chen¹

Received: 31 October 2018 / Published online: 12 November 2019
© The Author(s) 2019

Abstract

Tight sandstone gas (hereafter “tight gas”) has become a subject of unconventional gas exploration globally. The large-scale development and use of tight gas resources in the USA, in particular, facilitated the rapid rebound of natural gas production in the USA, in addition to driving the rapid development of tight gas worldwide. In the eastern Ordos Basin, the Upper Paleozoic feature includes multiple layers of gas, a shallow depth, and notable potential for exploration and development. However, the reservoirs in the area are relatively tight, exhibit strong heterogeneity, and possess a complex micropore structure, thus restricting the effective economic development of oil and gas. Thus, research on the primary parameters controlling pore throat structure and the seepage capability of low-permeability reservoirs will be beneficial for the efficient exploration and development of natural gas in the eastern Ordos Basin. The parameters of reservoir porosity and percolation ability, as well as permeability, were analyzed using systematic sampling of the of the Upper Paleozoic Benxi, Taiyuan, and Shanxi Formations in the eastern Ordos Basin, constant-rate mercury injection experiments, nuclear magnetic resonance analysis, and gas–water-phase experimental studies. The results indicate that reservoir porosity is controlled by the effective pore volume and number, whereas permeability is controlled by the largest throat radius, rather than the average. The effective pore volume controls the movable fluid saturation, while reservoir percolation capability is controlled by the effective pore volume, irreducible water saturation, and size of the gas–water two-phase seepage zone.

Keywords Porosity and permeability · Largest throat radius · Movable fluid saturation · Effective pore throat volume · The range of gas–water two-phase seepage zone

1 Introduction

In recent years, oil and gas researchers have shifted their focus from high-quality reservoir to tight reservoirs and from local trap exploration to large-area exploration and the whole basin. Therefore, the exploitation of unconventional energy has become critical in current explorations (Liu et al. 2013; Zou et al. 2013a, b, 2015a, b; Jia et al. 2014; Cao et al. 2017;

Yang et al. 2017; Song et al. 2018; Zhang et al. 2018). Tight gas and tight oil are the most realistic pending exploitation of unconventional oil and gas resources in China (Ma 2004; Jiang et al. 2015). Because of the flow of gas and water among the connected pores in the reservoir, the pore structure characteristics of the reservoir (the geometry, size, distribution, and interconnectivity of pores and throats) affect the flow of fluids in the reservoir significantly. Conventional gas reservoirs generally exhibit a clear gas–water interface, and porosity and permeability values are the primary physical parameters of conventional reservoir evaluation. The most remarkable characteristic of unconventional gas reservoirs is the absence of a clear gas–water interface, primarily non-Darcy seepage, complex seepage characteristics, strong reservoir heterogeneity, small pore throat, and diverse types. Some limitations exist in evaluating the reservoir performance and seepage ability of unconventional reservoirs using conventional porosity and permeability parameters.

Edited by Jie Hao

✉ Bo Yang
yangb_nwu@163.com

¹ State Key Laboratory of Continental Dynamics, Department of Geology, Northwest University, Xi’an 710069, Shaanxi, China

² Changqing Oilfield Company, PetroChina, Xi’an 710018, Shaanxi, China

A large number of exploration and development practices and research results have indicated that the complex seepage characteristics of tight sandstone gas reservoirs are the primary factors affecting the productivity and development of gas wells, and the difference in microscopic pore structure will result in differences in fluid flow state and distribution. Even if the porosity and permeability are close to each other, the seepage characteristics may be different because of the difference in pore structure, which may affect the productivity and development effect of gas reservoirs and ultimately affect oil recovery. Therefore, studies on the pore and throat structures and oil and gas seepage mechanism of ultralow porosity and ultralow-permeability tight reservoirs in the Ordos Basin are important and must be performed in gas exploration and exploitation. Predecessors performed considerable research and achieved remarkable progress in this area. Such achievements include identifying the different types of reservoir petrologic features (Fu et al. 2013; Luo et al. 2014), microscopic pore structures, evolution characteristics (Liu et al. 2006; Sakhaee-Pour and Bryant 2014), seepage characteristics, and controlling factors (He et al. 2008; Christopher et al. 2012). Generally, the current research on micropore characteristics is only a simple description of the experimental phenomena and does not effectively combine the differences in micropore structure to analyze its seepage characteristics; thus, systematic analysis of the primary characterization parameters of the pore permeability and seepage capacity of tight gas reservoirs is lacking.

Therefore, this paper taking the Upper Paleozoic in eastern Ordos Basin as the research object, the samples of Benxi Formation, Taiyuan Formation, and Shanxi Formation of Upper Paleozoic are collected systematically. On the basis of constant-rate mercury injection experiments (CRMI) and nuclear magnetic resonance (NMR) experiment, the micropore structure of reservoir is studied. Combined with gas–water relative seepage experiment, the controlling factors of different sandstone porosities and permeabilities are discussed and the pore structure's influence on reservoir permeability is analyzed comprehensively. The research results have important theoretical significance for understanding the seepage mechanism of ultra-low porosity and ultralow-permeability reservoirs and provide scientific basis for efficient development of the study area.

2 Regional geological outline

The Ordos Basin is the second largest sedimentary basin in China, with an area of about 3.7×10^5 km²; it is located in Midwest China and spans from the Lvliang Mountains in the east to the Tengger Desert in the west, respectively, with Yinshan and Qinling Mountains at its north and south ends.

Across the five provinces of Shaanxi, Gansu, Ningxia, Inner Mongolia, and Shanxi, the Ordos Basin appears as a large, multicycle cratonic basin with a simple structure. A number of tight gas fields have been found in the basin. These gas fields include the Sulige, Wushenqi, Daniudi, Shenmu, and Yulin gas fields, which account for 84% of the total natural gas reserves found in the basin, showing its rich and tight gas resources (Fu et al. 2004; Yang et al. 2012, 2014; Zou et al. 2015a, b; Yang et al. 2016; Lv et al. 2017). The study area is located in the eastern part of the basin with an area of 45,000 km² (Fig. 1), lying north from Yijinhuluo, south of Ansai, west of Hengshan, and east of Fugu. The main research strata comprise the Upper Paleozoic Benxi Formation, Taiyuan Formation, and Shanxi Formation, of which Shanxi Formation can be divided into Shan 1 member and Shan 2 member from the top to bottom.

3 Samples and experimental measurements

3.1 Samples

The primary rock types of the sandstone reservoir in study area are lithic quartz sandstone, and quartz sandstone. To ensure the representativeness of the core samples, 40 samples with different granule sizes and lithology were collected from the Benxi, Taiyuan, and Shanxi Formations, of which 10 were used for a constant-rate mercury injection (CRMI), 10 for the gas–water relative seepage experiment, and 10 for nuclear magnetic resonance (NMR) analysis.

3.2 Experimental measurements

The CRMI experiment presses the non-wetting phase of mercury into the sample at a low constant velocity. In quasi-static mercury injection, mercury will cause an increase in capillary pressure as it enters a relatively narrow space (such as a throat); when it enters a relatively large space (such as pores), the capillary pressure decreases. By measuring the fluctuation of the mercury intrusion pressure, the pores can be separated from the throats to achieve the measurement of the throats (Wang et al. 2018a, b). As an important rock test method, NMR analysis uses the frequency distribution of the transverse relaxation time T_2 of the sample to reflect the volumes of the pore and throat. Generally, the smaller the pore and throat spaces are, the larger the specific surface of the rock and the shorter the transverse relaxation time.

To ensure the comparability of experimental results among different measurements, each sample was cut into plugs and followed a specially designed experimental process. The core plugs were used for NMR and CRMI analyses and the gas–water relative seepage experiment.

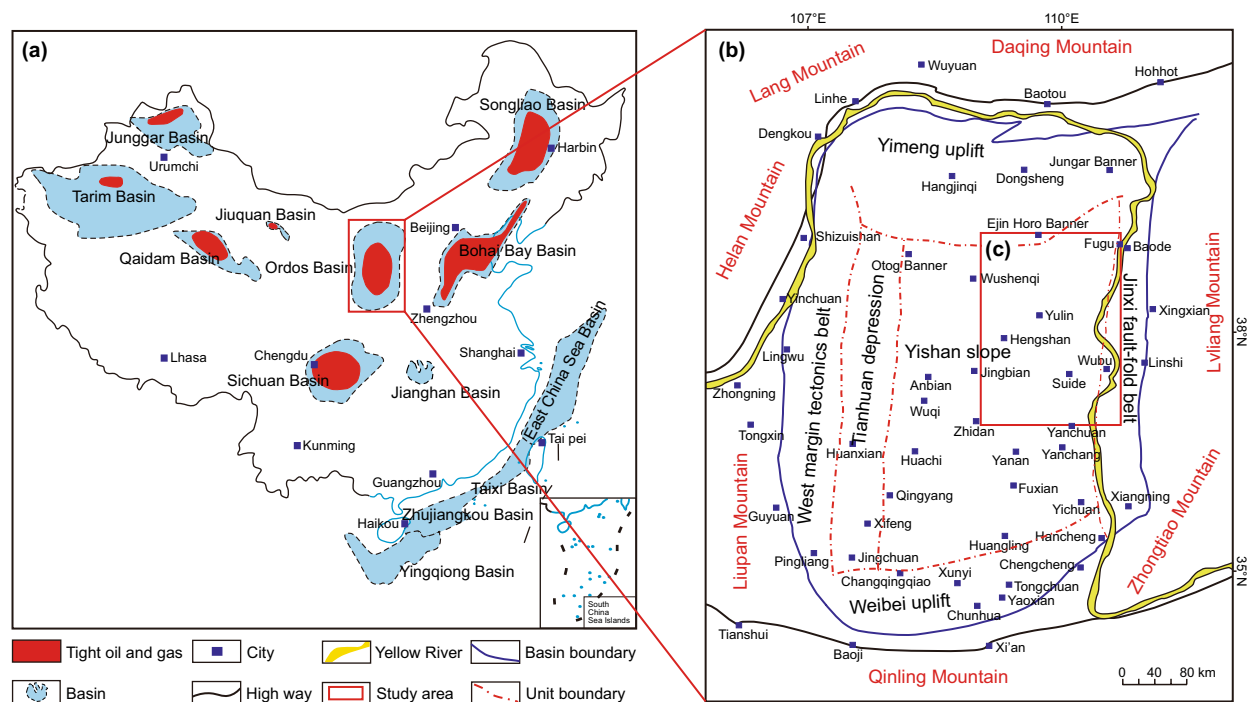


Fig. 1 Tight reservoir distributions in China and structural sketch map in the study area. **a** Tight reservoir distributions in China (after Jia et al. 2012). **b** Structural unit subdivision map of Ordos Basin and periphery. **c** Structural sketch map in the study area

3.2.1 NMR experiments

Before the experiments, the two sides of all samples were polished and cleaned to remove the remnants of the reservoir fluids or drilling mud inside the core samples. Subsequently, the samples were dried at 110 °C for at least 24 h until the weight of the core samples was constant. The weight of the core was subsequently measured, weighted, and vacuumed in simulated formation water (with a total salinity of 10,000 mg/L). After the full saturation of the core samples, the T2 spectra and NMR porosities were obtained. Subsequently, all movable water inside the pores were fully centrifuged, in which state another T2 spectra and NMR porosities were obtained. The NMR experiment was conducted by the National Development and Reform Commission Standard (SY/T)6490-2014. To achieve a good signal-to-noise ratio, the pulse sequence was set with the following parameters. The number of scan was set as 128, and the number of echoes was fixed as 4096 or 8192. The echo time and waiting time were chosen as 0.2 ms and 6 s, respectively. The experiment temperature was 35 °C.

3.2.2 CRMI experiments

The apparatus used for the CRMI experiments was the ASPE-730 Automated Pore System Examination. The CRMI experiment was conducted by the National Development and

Reform Commission Standard (SY/T) 5346-2005. The maximum intrusion pressure was 6.2 MPa (900 psi), corresponding to the minimum value of the throat radius (0.12 μm). The contact angle is 140°, and the interfacial tension is 485 dyn/cm. The temperature is 25 °C.

3.2.3 Gas–water relative seepage experiment

The gas–water relative seepage experiment was conducted according to the National Development and Reform Commission Standard (SY/T) 5345-2007. Nitrogen and water were used at normal temperature and normal pressure conditions. The temperature was 28 °C. The salinity of the formation water was 142,000 mg/L.

4 Results

4.1 Reservoir porosity–permeability characteristics by casting thin section

According to the statistical analysis of numerous casting thin sections (Table 1, Fig. 2), the reservoir porosity of Shanxi Formation, Taiyuan Formation, and Benxi Formation in the Upper Paleozoic of the eastern Ordos Basin is primarily distributed between 3.06% and 16.29%. The reservoir permeability is primarily distributed between 0.001

Table 1 Reservoir physical property statistical table in the research area

Formation	Number of wells	Number of samples	Porosity, %	Permeability, mD
Shanxi Formation				
Shan1 Member	108	3408	5.08	0.37
Shan2 Member	263	8610	5.05	0.51
Taiyuan Formation	113	5018	6.24	0.36
Benxi Formation	50	968	5.31	0.41

and 58.82 mD, with an average porosity of approximately 5%, except for Taiyuan Formation, whose permeability is slightly higher than those of the other strata at an average permeability of approximately 0.4 mD. The permeability of the Shan 2 member is slightly higher than those of the other formations. According to the oil and gas industry standards of Zhao et al. (1998), the reservoirs in the study area are typically ultralow-porosity and ultralow-permeability reservoirs. However, tight gas reservoirs present difficulties in the complete identification of the stand or the fall of reservoirs through porosity–permeability and the study methods of conventional reservoirs.

4.2 Reservoir pore throat structure characterized by CRMI experiment

The conventional mercury injection method cannot accurately distinguish the pore and throat structures. However, the constant-rate mercury injection technique can directly measure the distribution of the pore and throat, throat radius, pore radius, and the ratio of pore and throat radius, which can reflect the pore and throat characteristics of the rock samples (Zhao et al. 2015; Xi et al. 2016; Wu et al. 2017; Xiao et al. 2018; Zhang et al. 2017; Wang et al. 2018a, b). Ten samples from the eastern Upper Paleozoic reservoirs in the Ordos Basin were tested by the CRMI technique. Table 2 lists the physical parameters of the experiment.

4.3 Reservoir seepage characteristics by gas–water relative seepage experiment

The tight gas reservoir is characterized by poor physical properties, a complex micropore structure, and high water saturation, stress sensitivity, and capillary pressure, all of which affect the flow of gas, causing differences between the seepage characteristics of tight gas reservoirs and conventional gas. Under a high-speed flow, the gas seepage follows a non-Darcy binomial seepage law. The primary expression parameters of the seepage capability of tight gas reservoirs include irreducible water saturation and movable fluid saturation.

Twenty cores of reservoir rocks in the research area were tested by the gas–water relative seepage test (Table 3). The results indicated that the irreducible water saturation of the sample in the study area was primarily distributed between 17.50% and 78.63%, with an average of 50.65%. The conventional reservoirs generally exhibit a low irreducible water saturation, high movable fluid saturation, and remarkable reservoir seepage capability. However, the reservoirs in the study area are characterized by high irreducible water saturation, low movable fluid saturation, and poor seepage capability, which are properties of typical tight reservoirs.

4.4 Reservoir seepage characteristics by NMR experiment

Movable fluid saturation is another intuitive controlling factor of reservoir seepage capability, and it can be obtained by NMR experiments. Thus, the influencing factors of movable fluid saturation can be analyzed. Ten samples of reservoir rocks in the research area were tested in the NMR experiments (Table 4). The results indicated that the movable fluid saturation of the sample in study area was primarily distributed from 34.23% to 87.94%, and each stratum demonstrated no significant difference. According to the movable fluid saturation, the study area samples can be divided into four types. No significant correlation is observed between the movable fluid saturation and reservoir porosity–permeability, indicating that the reservoir seepage capability is not controlled by conventional physical parameters.

5 Discussion

5.1 Primary controlling parameters of porosity and permeability

CRMI can measure the pores and throats separately. Thus, the intrusion curves of the total, pore, and throat are recorded simultaneously. The pore radius distribution of the samples in the study area is 0–400 μm with the primary range of 100–200 μm . No significant difference is observed in the pore radius of samples of different permeabilities (Fig. 3), indicating that the difference in pore throat structure in low-permeability sandstone is primarily reflected in the throat. Meanwhile, the throat controls the reservoir properties and seepage capability. Figures 4 and 5 show that the reservoir porosity is controlled by a unit volume of the effective pore throat volume and number.

The throat radius of the samples in the research area ranged from 0.4 to 4.5 μm . The throat radii of the samples with different permeabilities differed significantly, and the throat distribution widened with increasing permeability (Fig. 6). The correlation between the maximum

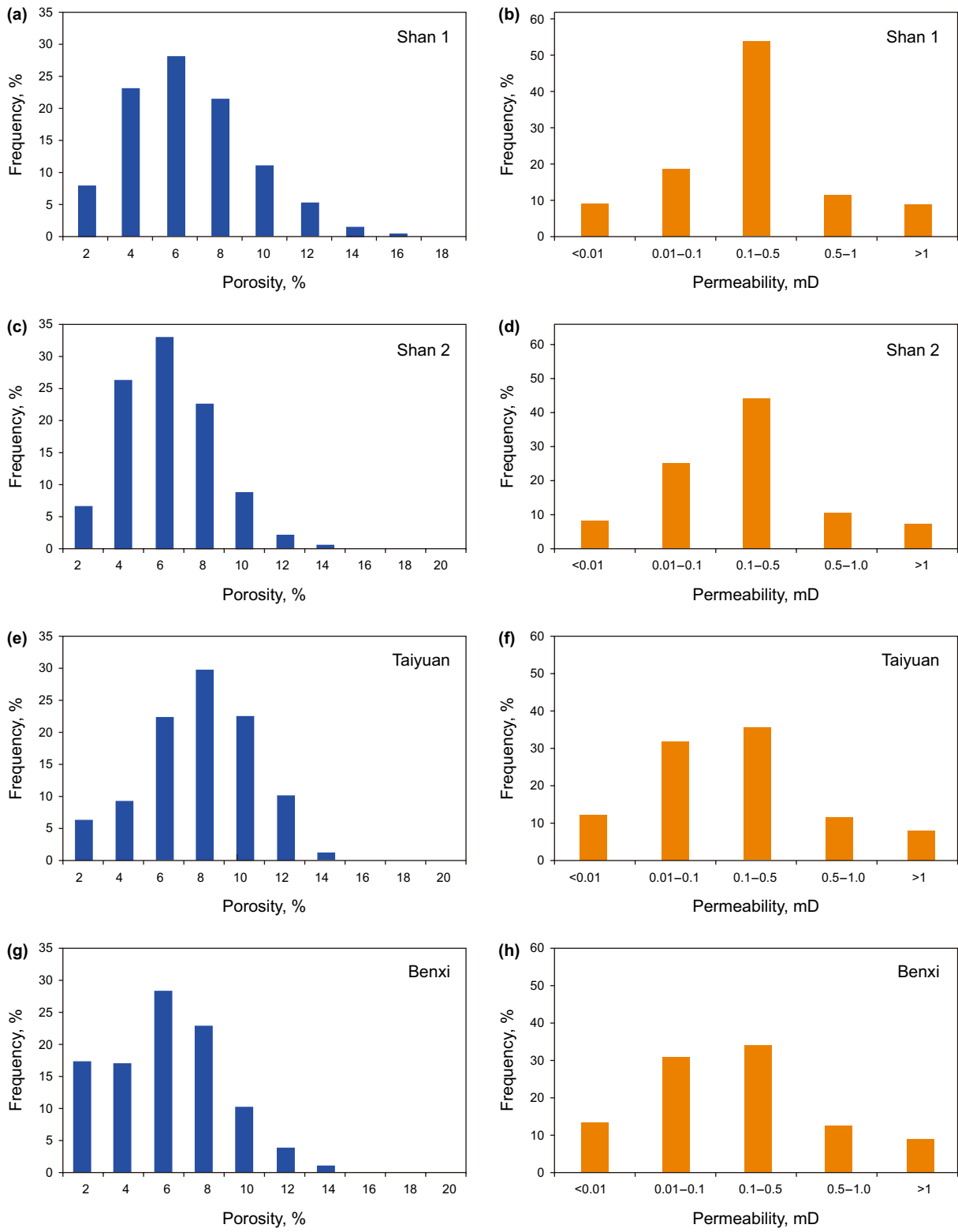


Fig. 2 Porosity–permeability frequency histogram of each formation in research area

Table 2 Constant-rate mercury injection sample physical property parameter table

Well	Depth, m	Formation	Porosity, %	Permeability, mD	Density, g/cm ³	Volume, cm ³	Pore volume, cm ³
Fu4	2305.30	Shan 1	12.60	2.77	2.33	2.62	0.33
Shaan394	2901.36	Shan 1	3.5	0.39	2.57	4.86	0.17
Shuang3	2778.32	Shan 2	8.8	0.66	2.40	3.65	0.32
Mi9	2651.68	Shan 2	9.6	0.73	2.41	3.54	0.34
Yu86	2619.62	Shan 2	6.4	1.23	2.47	3.35	0.21
Shuang95	2472.69	Taiyuan	8.5	0.33	2.47	3.54	0.30
Shuang3	2824.98	Taiyuan	10.7	1.09	2.38	3.06	0.33
ZhenChuan8	2282.50	Taiyuan	9.7	1.73	2.43	3.17	0.31
Tong12	2977.96	Benxi	8.8	2.55	2.40	3.07	0.27
Shaan247	3266.11	Benxi	5.4	1.38	2.55	4.48	0.24

throat radius and permeability is better than that between the average throat radius and permeability, implying that the reservoir permeability is controlled by the maximum throat radius (Fig. 7).

In addition, the concept of injection mercury coefficient *S* is proposed herein; it can be used to quantitatively characterize the relationship between the pore and throat configurations of reservoirs. The injection mercury coefficient is computed as follows:

$$s = \frac{s_t - s_b}{S_{total}^2} \tag{1}$$

In the equation above, *S_t* refers to the injection mercury saturability of the throat, *S_b* denotes the injection mercury saturability of the pore, and *S_{total}* represents the final injection mercury saturability. Reservoirs can be divided into pore-type and throat-type reservoirs based on the injection mercury coefficient and mercury injection curve characteristic, respectively. A pore-type reservoir is observed when *S* < 0, and the total pore injection mercury saturability is higher than the total throat injection mercury saturability. The reservoir is a throat type when *S* > 0, with the total throat mercury saturability being higher than the total pore mercury saturability. A larger *S* value results in a more notable control effect of the throat and poorer reservoir conditions. In the research area, Taiyuan Formation is a pore type, Shan 1 member is a throat type, and Shan 2 member and Benxi Formation exhibit both reservoir types (Table 5). Figure 8 shows the poor correlation between the total injection mercury saturability of the throat and the total injection mercury saturability, and the high correlation between the total injection mercury saturability of the pore and the total injection mercury saturability, indicating that the reservoirs are primarily the pore type.

According to the experimental parameters of CRMI, the combination of the injection mercury coefficient and mercury injection curve characteristics can be used for the specific quantitative characterization of pore-type and throat-type reservoirs. As shown in Fig. 9, when the throat is large, the injection mercury amount is primarily controlled by the throat; on the contrary, it is controlled by the pore. However, given the small number of large throats, this parameter features minimal contribution to the injection mercury amount, implying that the injection mercury amount is primarily controlled by the pore.

Pore-type reservoirs are primarily controlled by the throat when the throat radius > 3 μm but jointly controlled by the pore and throats between 1.8 and 3 μm. The reservoir is controlled by the pore when the throat radius < 1.8 μm. The figure presents the small contribution of the throat; that is, the injection mercury amount is primarily controlled by the pore. Meanwhile, the throat-type reservoirs are primarily controlled by the throat when the throat radius > 1.5 μm, but they are controlled by the pore and throat between 0.8 and 1.5 μm. The throat-type reservoir is controlled by the pore when the throat radius < 0.8 μm. The figure shows the small contribution of the pores. Thus, the injection mercury amount is primarily controlled by the throat (Table 6).

In summary, the reservoir is a pore type when the injection mercury coefficient < 0. Meanwhile, the reservoir is controlled by the pore when the throat radius < 1.8 μm. When the injection mercury coefficient > 0, the reservoir is a throat type. Meanwhile, the reservoir is controlled by the throat when the throat radius > 1.5 μm. Thus, according to the analysis of the correlation between the constant-rate mercury injection experiment parameters and the porosity and permeability (Table 7), the porosity is controlled by the per unit volume of the effective pore throat volume and number,

Table 3 Gas–water relative seepage experiment results data sheet in the research area

Formation	Well	Depth, m	Gas-measured permeability, mD	Porosity, %	Irreducible water		Intersection point		Residual gas	
					Water saturation, %	Residual water–gas-phase permeability, mD	Water saturation, %	Gas–water relative permeability, mD	Water saturation, %	Water relative permeability, mD
Shan 1	Yu5	2050.71	0.11	3.68	78.63	0.002	87.7	0.185	93.59	0.436
	Fu4	2304.10	0.68	13.40	76.82	0.066	85.5	0.420	92.68	0.731
Shan 2	Shaan394	2899.89	0.19	2.32	70.65	0.026	85.6	0.270	86.59	0.342
	Shuang3	2779.90	0.55	9.10	38.96	0.260	56.0	0.280	73.29	0.693
	Mi9	2652.68	0.51	8.34	67.33	0.042	80.2	0.290	90.55	0.631
	Yu86	2621.16	0.18	2.78	59.33	0.038	80.6	0.315	84.51	0.44
Taiyuan	Tong12	2912.45	46.3	9.76	34.55	13.30	57.4	0.225	75.16	0.547
	Tong29	2857.08	0.12	2.63	72.01	0.002	82.3	0.12	86.01	0.283
	Shaan143	2797.43	0.3	4.81	72.01	0.025	84.3	0.305	89.01	0.552
	Shaan257	3104.22	1.48	7.44	21.51	1.590	42.6	0.170	65.11	0.602
	Shaan247	3169.01	0.16	3.61	26.19	0.032	50.7	0.245	68.77	0.572
	Shuang3	2826.91	0.89	10.90	46.34	0.117	59.2	0.215	84.22	0.877
	Fu4	2408.16	0.24	6.60	57.24	0.031	73.8	0.315	83.87	0.623
	Yu72	2777.53	0.62	9.02	34.82	3.480	60.5	0.110	74.22	0.375
	Shuang95	2471.45	0.12	7.46	45.95	0.012	43.2	0.327	80.93	0.831
	Tong29	2885.71	0.61	9.93	46.72	0.079	38.6	0.315	83.03	0.823
Benxi	Tong12	2979.40	4.08	6.71	34.01	1.670	58.3	0.264	73.10	0.584
	Mi9	2749.08	0.29	6.29	17.50	0.116	40.3	0.287	67.00	0.675
	Shaan247	3265.09	6.42	9.12	61.73	6.110	78.8	0.315	79.96	0.349

Table 4 Nuclear magnetic resonance data and the results of the analysis in the research area

Well	Formation	Depth, m	NMR porosity, %	Gas-measured permeability, mD	Water-measured porosity, %	The movable fluid saturation, %	The movable fluid porosity, %	The irreducible water saturation, %	The classification of movable fluid saturation
Shuang3	Shan 2	2778.32	8.98	0.66	8.68	68.19	6.13	31.81	I
Yu86	Shan 2	2617.68	7.74	1.23	7.29	87.94	6.81	12.06	I
Tong12	Benxi	2979.28	7.66	2.55	7.54	87.66	6.72	12.34	I
Shuang95	Taiyuan	2471.93	7.40	0.33	7.25	50.49	3.73	49.51	II
Shuang3	Taiyuan	2824.76	11.10	1.09	11.03	61.65	6.84	38.35	II
ZhenChuan8	Taiyuan	2280.03	8.42	1.73	8.21	61.30	5.16	38.70	II
Fu4	Shan 1	2305.10	12.16	1.77	11.87	42.31	5.15	57.69	III
Shaan394	Shan 1	2898.85	5.26	0.39	5.24	36.05	1.90	63.95	II
Mi9	Shan 2	2652.08	10.62	0.48	10.41	34.29	3.64	65.71	IV
Shaan247	Benxi	3266.11	7.77	1.38	7.60	34.23	2.66	65.77	IV

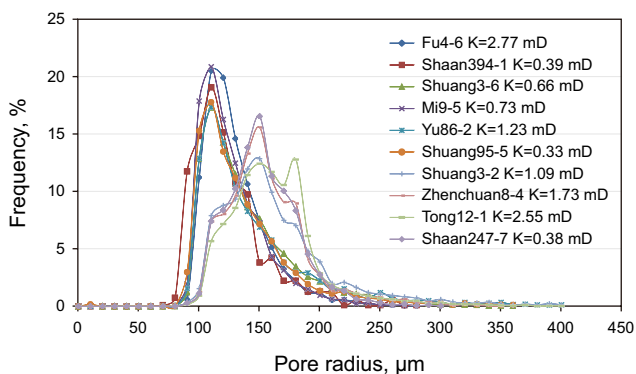


Fig. 3 Pore radius distribution frequency diagram in the research area

whereas the reservoir permeability is controlled by the largest throat radius.

5.2 Primary controlling parameters of reservoir seepage capability

The experimental methods used in this study are the gas–water relative seepage experiment and NMR analyses. The former can reflect the interference degree of the gas–water phase, while the latter can quantitatively reflect the movable fluid saturation and movable interval.

5.2.1 Characterization of the reservoir seepage capability by the gas–water relative seepage experiment

Given the complex two-phase gas–water seepage of tight gas reservoirs, the study on the rule of reservoir fluid seepage is important (Zeng et al. 2010). Intuitively, gas–water

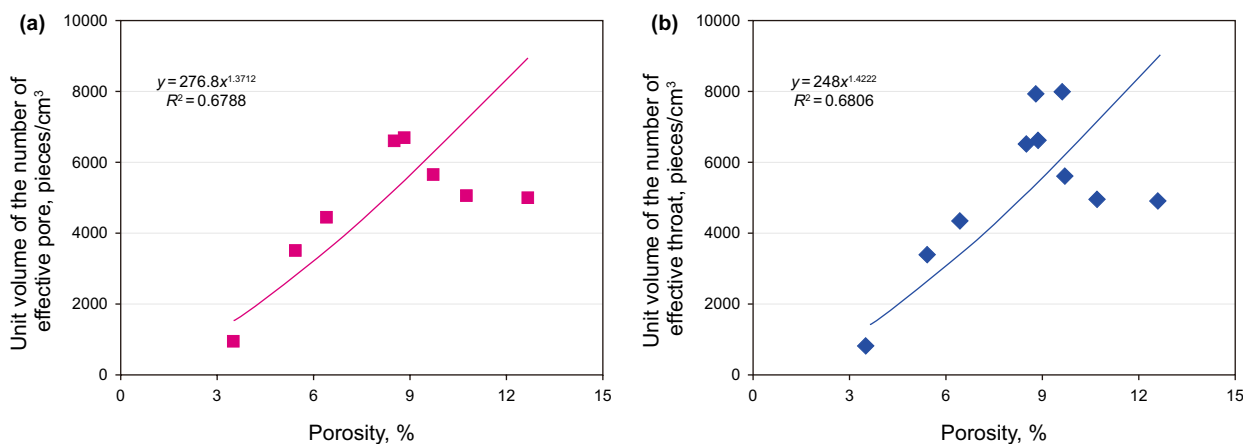


Fig. 4 Per unit volume of the number of effective pore-throat and porosity diagram in the research area

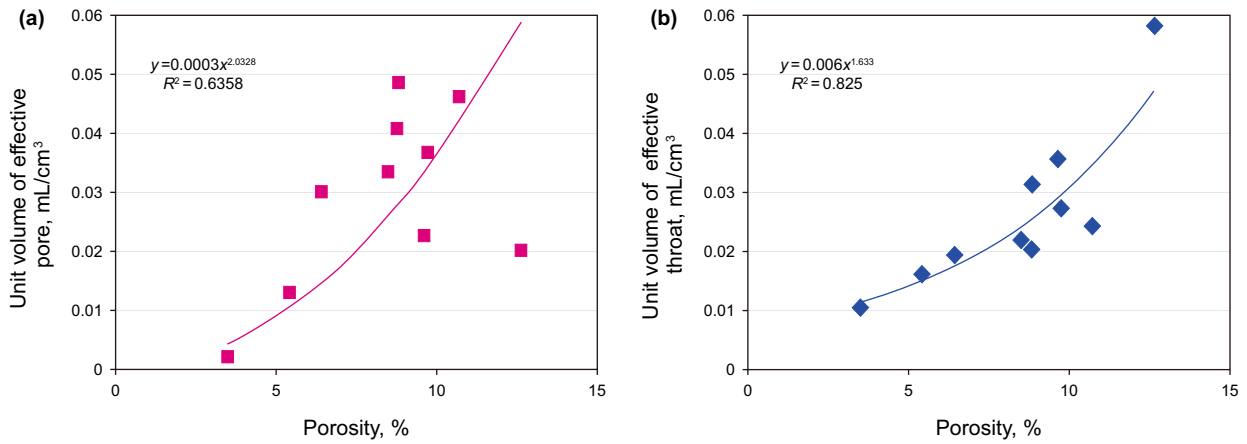


Fig. 5 Per unit volume of effective pore-throat volume and porosity diagram in the research area

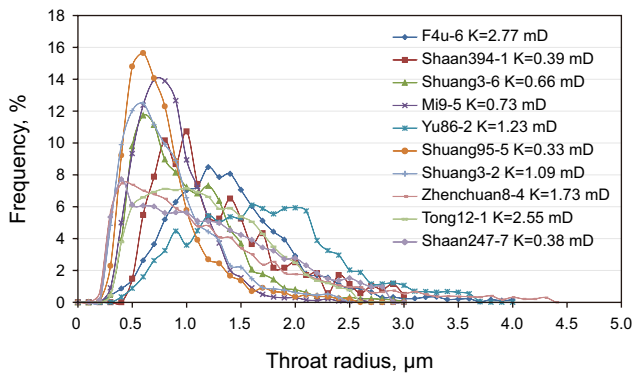


Fig. 6 Throat radius distribution frequency diagram in the research area

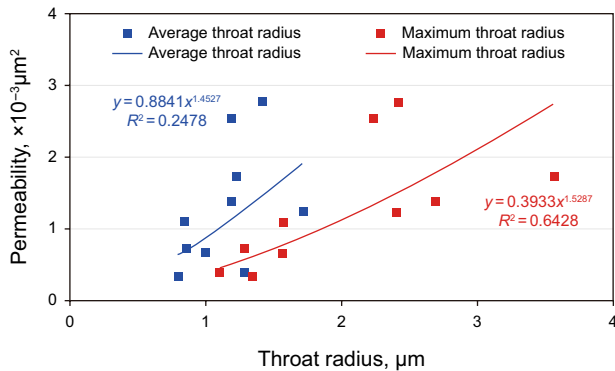


Fig. 7 Average throat radius and permeability relationship diagram in the research area

relative seepage curves can provide reference for the microcosmic seepage characteristics of reservoirs in the research area (Zeng et al. 2005; Gharbi and Blunt 2012; Li et al. 2012).

The gas–water relative seepage curves of 20 cores were measured in this study, and the results are shown in Table 3. The range of irreducible water saturation of the sample in the study area is 17.50%–78.63%, with an average of 50.65%. Meanwhile, the irreducible water saturation of 20 samples is higher than the residual gas saturation, indicating hydrophilicity. The isotonic point saturation ranges from 38.6% to 87.7%, with an average of 65.6%, indicating that the water phase must reach a higher rock porosity to reach the level of gas-phase seepage capability when $S_{wx} > 50\%$, implying rock hydrophilicity.

For the gas–water relative seepage curves, the three characteristics endpoints were as follows: S_{wi} was the irreducible water saturation point (A point), S_{gr} was point of residual gas saturation (C point), and an isotonic point (B point) was observed, indicating the intersection of two curves (Zhang 2014). These endpoints can be connected to form a triangle referred to as a seepage triangle (Fig. 10a). The different characteristics of tight gas reservoir seepage often appeared, to a certain extent, as changes in the relative position and shape of the seepage triangle. In general, the seepage triangle was positioned more to the right of the same coordinate axis, and reservoirs with poor conditions were observed. The lengths of AB and BC represent the interference degrees of the gas–water phase. Typically, a shorter AB length indicates a stronger degree of water-phase interference. The length of AC represents the two-phase seepage range. Thus, a longer length denotes a greater seepage range. BD refers to the height of the triangular, whereas the length represents the level of the isotonic point. A higher point signifies a stronger gas–water seepage. By comparing the triangle shape of the gas–water relative seepage curves in the research area, four primary types of seepage triangles were identified (Fig. 10b).

Considering the endpoints of the curves (the characteristics of seepage triangle, relative permeability ratio, and slope of water saturation ratio curve), the gas–water

Table 5 Constant-rate mercury injection capillary pressure curve characteristic parameters

Pore throat characteristic parameter	Shan 1 Formation		Shan 2 Formation			Taiyuan Formation			Benxi Formation	
	Fu4	Shaan394	Shuang3	Mi9	Yu86	Shuang95	Shuang3	ZhenChuan8	Tong12	Shaan247
Displacement pressure, MPa	0.31	0.67	0.47	0.57	0.31	0.55	0.47	0.21	0.33	0.27
Permeability, mD	2.77	0.39	0.66	0.73	1.23	0.33	1.09	1.73	2.55	1.38
Pore throat volume ratio	0.34	0.19	1.31	0.64	1.6	1.55	1.93	1.37	2.45	0.82
Final mercury saturation S_p , %	61.9	34.43	81.59	60.54	76.11	64.57	65.34	65.45	77.78	52.66
Total pore mercury saturation S_b , %	15.77	5.56	46.35	23.55	46.86	39.20	43.00	37.78	55.21	23.70
Total throat mercury saturation S_t , %	46.08	28.87	35.25	37.00	29.25	25.36	22.34	27.67	22.56	28.96
Mercury coefficient S	0.79	1.97	-0.17	0.37	-0.30	-0.33	-0.48	-0.24	-0.54	0.19

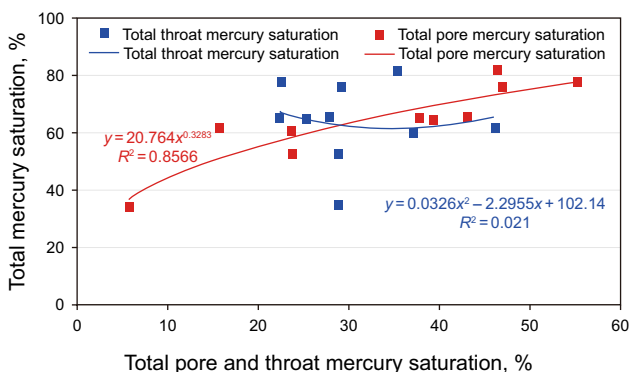


Fig. 8 Diagram between total pore throat mercury intrusion saturation and total mercury saturation

relative seepage curves can be classified from good to poor into class I (low irreducible water saturation, wide two-phase zone, and poor interference level of gas and water), class II (lower irreducible water saturation, wider two-phase region, and poorer interference level of gas and water), class III (high irreducible water saturation, narrow two-phase region, and strong interference level of gas and

water), and class IV (higher irreducible water saturation, narrower two-phase region, and stronger interference level of gas and water) (Fig. 11, Table 8).

The ratio of relative permeability of gas to water reflects their seepage ability and interference degree in a two-phase fluid. It is exponentially related to water saturation (S_w) (Fig. 12). The correlation formula is as follows:

$$\frac{K_{rg}}{K_{rw}} = ae^{-bS_w} \tag{2}$$

In the equation, a and b are constants related to reservoir and fluid properties, respectively. Therefore, in gas reservoir exploitation, with the decrease in production pressure, the water cut begins to rise, and the seepage law changes. The theory of seepage in medium- and high-permeability gas reservoirs is no longer applicable because of the inflection point in the water flooding gas curve and the “discontinuous phase” seepage in the underground gas reservoir. For different samples, when S_w increases by the same percentage, the decrease in relative permeability ratio is different. The faster the decline, the worse the gas seepage capacity, and the larger the slope of the curve. On

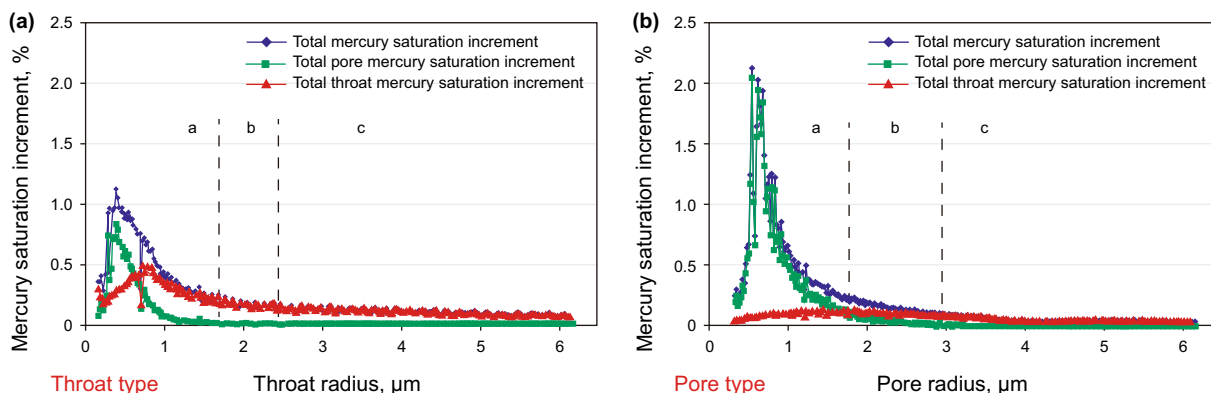


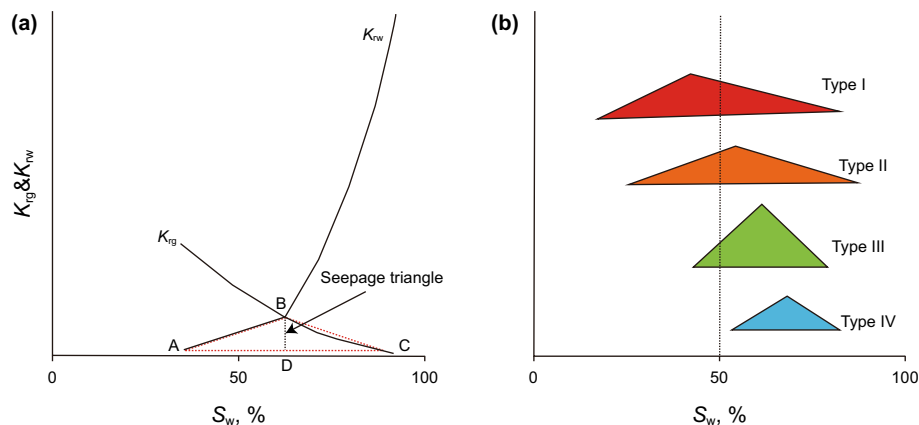
Fig. 9 The relation between pore/throat radius and the mercury saturation in the research area

Table 6 Constant-rate mercury injection experiment microscopic pore structure partition

Types	Throat type			Pore type		
	<0.8	0.8–1.5	>1.5	<1.8	1.8–3	>3
The scope of pore throat radius (μm)						
Constant-rate mercury injection experiment	Pore master area (a area)	Pore throat master area (b area)	Throat master area (c area)	Pore master area (a area)	Pore throat master area (b area)	Throat master area (c area)

Table 7 Correlation between constant-rate mercury injection experiment parameters and porosity and permeability tables

Constant-rate mercury injection experiment parameters	Porosity, %		Permeability, mD	
	R^2	Correlation	R^2	Correlation
Microcosmic pore throat characteristic parameters				
The mean pore radius	0.066	Power	0.254	Logarithmic
The mean throat radius	-0.101	Power	0.248	Power
The largest throat radius	0.071	Power	0.643	Power
The mean pore throat radius ratio	0.144	Power	-0.007	Exponential
Per unit volume of effective pore	0.636	Power	0.094	Exponential
Per unit volume of effective throat	0.825	Logarithmic	0.240	Linear
Per unit volume of the number of effective throat	0.680	Power	0.081	Power
Per unit volume of the number of effective pore	0.679	Power	0.077	Power
The total pore throat parameters				
The total pore mercury intrusion saturation	0.311	Power	0.081	Power
The total throat mercury intrusion saturation	0.136	Linear	0.056	Linear
The total mercury intrusion saturation	0.476	Power	0.154	Power

**Fig. 10** Classification based on relative seepage (Zhang 2014)

the contrary, the smaller the slope, the stronger the gas seepage capacity (Fig. 12).

Considering that a wider reservoir two-phase gas–water seepage zone indicates a lower irreducible water saturation, a better seepage capability of reservoirs can be achieved. To a certain extent, the reservoir seepage capability is controlled

by irreducible water saturation and the range of the two-phase gas–water seepage zone. The gas–water permeability curves of tight sandstone reservoirs in the study area are classified as type I and type II. The original water saturation varies widely, and the ratio of gas to water relative permeability decreases slowly with the increase in water saturation.

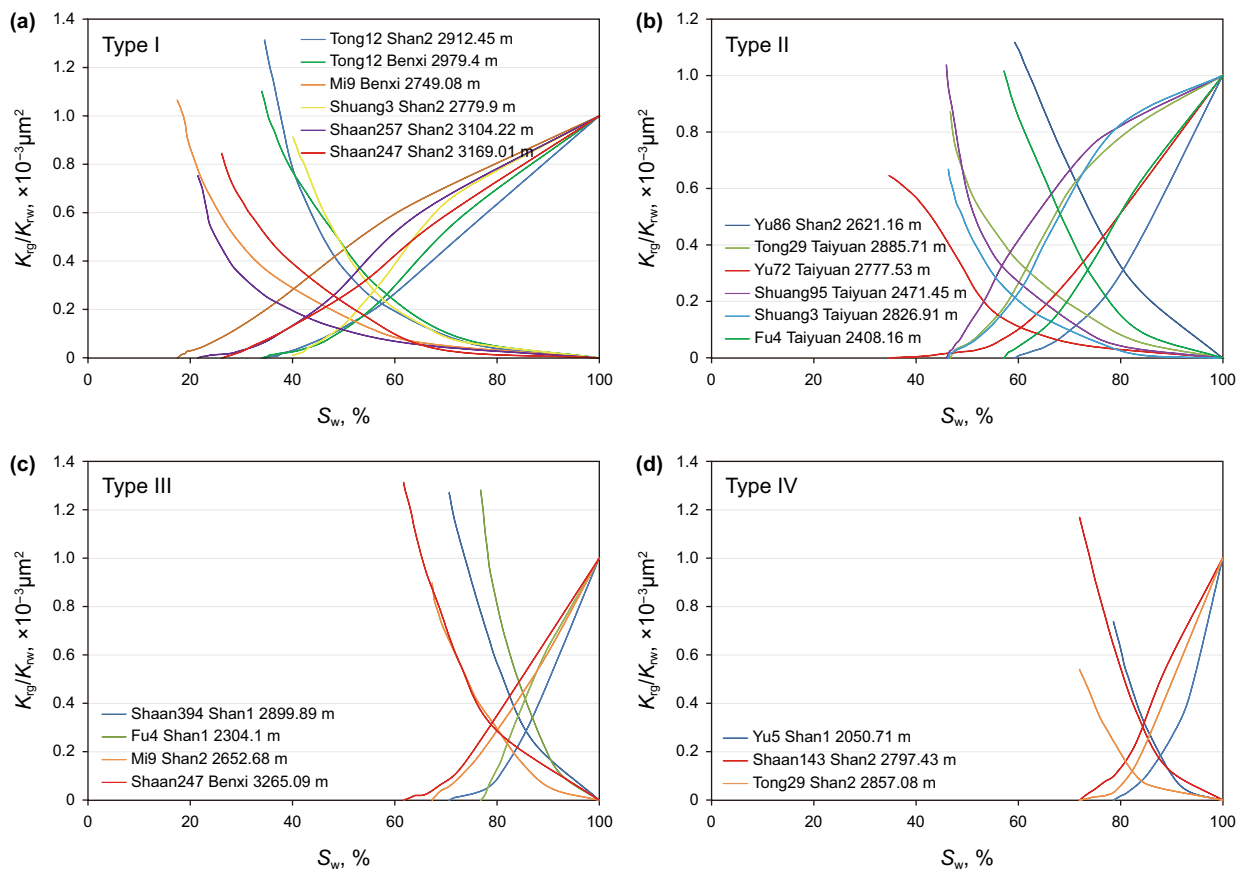


Fig. 11 Classification chart of gas–water-phase permeability curve

Table 8 Relative seepage analysis data

Classify	Bound water		Intersection point		Residual gas		Permeation area range, %
	Water saturation, %	Gas relative permeability	Water saturation, %	Gas relative permeability	Water saturation, %	Gas relative permeability	
I	28.79	2.82	50.88	0.245	70.41	0.61	41.62
II	57.79	1.63	70.7	0.294	84.16	0.56	29.37
III	73.76	0.01	85.2	0.191	88.73	0.35	26.78
IV	62.46	0.007	87.8	0.154	91.32	0.33	14.97

5.2.2 Characterization of reservoir seepage capability by movable fluid saturation

The ultralow-permeability sandstone reservoirs are jointly affected by the deposition and diagenesis, and feature complex microscopic pore structures and different fluid occurrences compared with the high-permeability reservoirs (Huyan et al. 2018; Lai et al. 2018a, b). Therefore, the quantitative evaluation of movable fluid saturation can represent the reservoir seepage capability to a certain degree and is crucial for the evaluation of ultralow-permeability

reservoirs (Gao and Sun 2010; Gao et al. 2010, 2014; Xie and Xiao 2011; Yang et al. 2016; Lai et al. 2018a, b).

To better evaluate the reservoir seepage capability, the microscopic pore structure parameters and the movable fluid saturation of the reservoirs were combined to analyze the primary controlling parameters of movable fluid saturation. Thereby, the fundamental control parameters of reservoir seepage capability can be ascertained (Table 9).

The results indicate the better correlation between the unit volume of the effective pore volume and movable fluid saturation than that between the unit volume of the effective

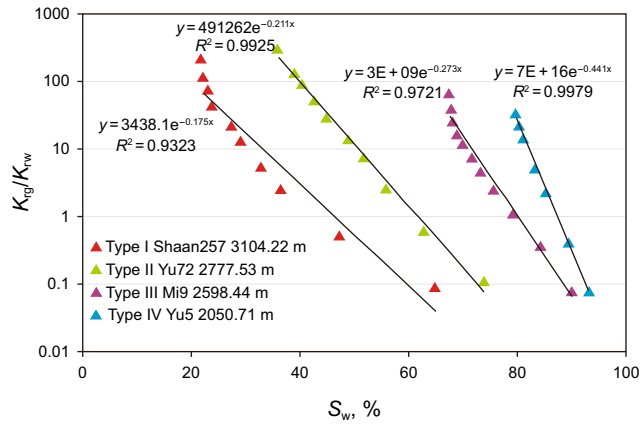


Fig. 12 Curves of relative permeability and S_w

throat volume and movable fluid saturation (Fig. 13), indicating that movable fluid saturation is controlled by the unit volume of the effective pore volume, whereas the unit volume of the effective throat volume is negligible. Therefore, the unit volume of the effective pore volume is a primary controlling parameter for the tight gas reservoir seepage capability.

6 Conclusions

1. According to the analysis of the characteristic parameters of microscopic pore throat by CRMI tests and the correlation between porosity and permeability, the reservoir porosity was controlled by the number and volume

of the effective pore and throat, whereas the permeability was controlled by the maximum throat radius rather than the average throat radius.

2. As determined by the NMR experiment and gas–water relative seepage experiment data and redefining the gas–water relative seepage curve, the movable fluid saturation was controlled by the unit volume of the effective pore volume, indicating that reservoir seepage capability was controlled by the unit volume of the effective pore volume, irreducible water saturation, and the range of the two-phase gas–water seepage zone.

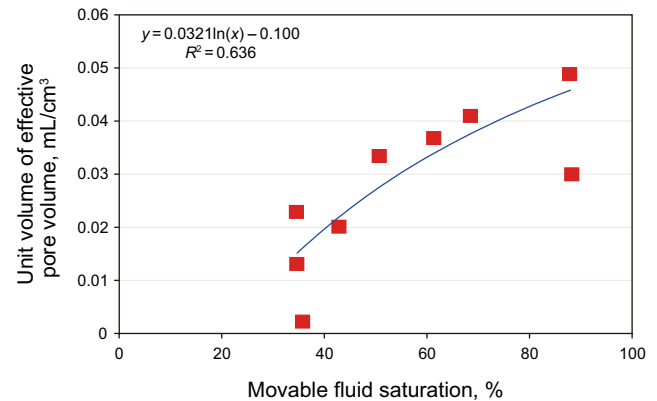


Fig. 13 Correlation between unit volume of effective pore volume and movable fluid saturation graph

Table 9 Linear correlation coefficient R^2 between movable fluid saturation and CRMI parameters

CRMI experimental parameters	Correlation coefficient between movable fluid saturation R^2
Microcosmic pore throat characteristic parameters	
The mean pore radius	0.328
The mean throat radius	0.101
The largest throat radius	0.005
The mean pore throat radius ratio	0.001
Per unit volume of effective pore	0.636
Per unit volume of effective throat	−0.033
Per unit volume of the number of effective throat	0.081
Per unit volume of the number of effective pore	0.080
The total pore throat parameters	
The total pore mercury intrusion saturation	0.761
The total throat mercury intrusion saturation	−0.170
The total mercury intrusion saturation	0.626

Acknowledgements This research was financially supported by the National Natural Science Foundation of China (Grants Nos. 41390451 and 41172101) and the National Key Research Project of China (No. 2016YFC0601003). We would like to appreciate the Changqing Oil-field Company of PetroChina for providing data collection. Our thanks are also extended to Department of Geology, Northwest University for supporting this paper. Finally, we would like to thank anonymous reviewers and the editors for their comments and suggestions.

Open Access This article is distributed under the terms of the Creative Commons Attribution 4.0 International License (<http://creativecommons.org/licenses/by/4.0/>), which permits unrestricted use, distribution, and reproduction in any medium, provided you give appropriate credit to the original author(s) and the source, provide a link to the Creative Commons license, and indicate if changes were made.

References

- Cao Z, Liu GD, Zhan HB, Gao J, Zhang J, Li C, et al. Geological roles of the siltstones in tight oil play. *Mar Pet Geol.* 2017;83:333–44. <https://doi.org/10.1016/j.marpetgeo.2017.02.020>.
- Christopher RC, Jerry LJ, Pedersen PK, Freeman M. Innovative methods for flow-unit and pore-structure analyses in a tight siltstone and shale gas reservoirs. *AAPG Bull.* 2012;96(2):355–74. <https://doi.org/10.1306/05181110171>.
- Fu JH, Xi SL, Liu XS, Liuyi S. Complex exploration techniques for the low-permeability lithologic gas pool in the Upper Paleozoic of Ordos Basin. *Pet Sci.* 2004;1(2):111–9.
- Fu JH, Wei XS, Nan JX. Characteristics and origin of reservoirs of gas fields in the Upper Paleozoic tight sandstone, Ordos Basin. *J Palaeogeogr.* 2013;15(4):529–38. <https://doi.org/10.7605/gdrlxb.2013.04.042> (in Chinese).
- Gao H, Sun W. Movable fluid changing characteristics and diversity origin of ultra-low permeability sandstone reservoirs—take the Yanchang Formation in Ordos Basin as an example. *Acta Geol Sin.* 2010;84(8):1223–30 (in Chinese).
- Gao SS, Ye LY, Xiong W, Guo H-K, Hu Z-M. Nuclear magnetic resonance measurements of original water saturation and mobile water saturation in low permeability sandstone gas. *Chin Phys Lett.* 2010;27(12):128902. <https://doi.org/10.1088/0256-307x/27/12/128902>.
- Gao H, Sun W, Pang ZY, Zhang R, Ma E. Movable fluid saturation of low-permeability and tight gas reservoir: taking He8 Section of Block Su 48 in Sulige Gas Field as an example. *Prog Geophys.* 2014;29(1):324–30. <https://doi.org/10.6038/pg20140146> (in Chinese).
- Gharbi O, Blunt MJ. The impact of wettability and connectivity on relative permeability in carbonates: a pore network modeling analysis. *Water Resour Res.* 2012;48(12):1–14. <https://doi.org/10.1029/2012wr011877>.
- He YM, Fan ZH, Sun SR. The situation and prospects of filtration mechanism in low permeability reservoirs. *Pet Geol Eng.* 2008;22(3):5–7. <https://doi.org/10.3969/j.issn.1673-8217.2008.03.002> (in Chinese).
- Huyan YY, Pang TS, Liu FJ, Jiang FJ, Chen XZ, Ma XQ, et al. Petrophysical characterisation of tight sandstone gas reservoirs using nuclear magnetic resonance: a case study of the upper Paleozoic strata in the Kangning area, eastern margin of the Ordos Basin, China. *Aust J Earth Sci.* 2018;65(6):863–75. <https://doi.org/10.1080/08120099.2018.1472664>.
- Jia CZ, Zhang M, Zhang YF. Unconventional hydrocarbon resources in China and the prospect of exploration and development. *Petrol Explor Devel.* 2012;39(2):129–36.
- Jia CZ, Zhang YF, Zhao X. Prospects of and challenges to natural gas industry development in China. *Nat Gas Ind.* 2014;34(2):8–18. <https://doi.org/10.1016/j.ngib.2014.10.001> (in Chinese).
- Jiang ZX, Li Z, Li F, Pang XQ, Yang W, Liu LF, et al. Tight sandstone gas accumulation mechanism and development models. *Pet Sci.* 2015;12(4):587–605. <https://doi.org/10.1007/s12182-015-0061-6>.
- Lai J, Wang GW, Wang ZY, Chen J, Pang X, Wang S, et al. A review on pore structure characterization in tight sandstones. *Earth Sci Rev.* 2018a;177:436–57. <https://doi.org/10.1016/j.earscirev.2017.12.003>.
- Lai J, Wang GW, Pang XJ, Fan X, Zhou Z, Si Z, et al. Effect of Pore Structure on Reservoir Quality and Oiliness in Paleogene Dongying Formation Sandstones in Nanpu Sag, Bohai Bay Basin, Eastern China. *Energy Fuels.* 2018b;32:9220–32. <https://doi.org/10.1021/acs.energyfuels.8b01989>.
- Li SQ, Zhang Y, Zhang X. Geologic modeling and fluid-flow simulation of acid gas disposal in western Wyoming. *AAPG Bull.* 2012;96(4):635–64. <https://doi.org/10.1306/07261110178>.
- Liu RE, Li WH, Chen MJ. Reservoirs evaluation and exploration prospect of the Member2 of Shanxi Formation of Lower Permian in eastern Ordos. *J Palaeogeogr.* 2006;8(4):531–8. <https://doi.org/10.3969/j.issn.1671-1505.2006.04.010> (in Chinese).
- Liu GD, Sun ML, Zhao ZY, Wang X, Wu S. Characteristics and accumulation mechanism of tight sandstone gas reservoirs in the Upper Paleozoic, northern Ordos Basin, China. *Pet Sci.* 2013;10(4):442–9. <https://doi.org/10.1007/s12182-013-0294-1>.
- Luo JL, Liu XS, Fu XY. Impact of petrologic components and their diagenetic evolution on tight sandstone reservoir quality and gas yield: a case study from He 8 gas-bearing reservoir of Upper Paleozoic in northern Ordos Basin. *Earth Sci J China Univ Geosci.* 2014;39(5):537–45. <https://doi.org/10.3799/dqkx.2014.051> (in Chinese).
- Lv CH, Huang WH, Fei L. The provenance analysis of the 8th member of the upper paleozoic Shihezi Formation in the western area of Ordos Basin. *Energy Sources Part A Recovery Util Environ Effects.* 2017;39(17):1886–93. <https://doi.org/10.1080/15567036.2017.1381786>.
- Ma XH. Exploration experience and problem concerning deep basin gas in the Ordos Basin. *Pet Sci.* 2004;1(2):62–8.
- National Development and Reform Commission. SY/T 5346-2005 Rock Capillary Pressure Measurement. Beijing: Petroleum Industry Press; 2005. p. 1–21 (in Chinese).
- Sakhaee-Pour A, Bryant SL. Effect of pore structure on the producibility of tight-gas sandstones. *AAPG Bull.* 2014;98(4):663–94. <https://doi.org/10.1306/08011312078>.
- Song ZZ, Liu GD, Yang WW, Zou H, Sun M, Wang X. Multi-fractal distribution analysis for pore structure characterization of tight sandstone—a case study of the Upper Paleozoic tight formations in the Longdong District, Ordos Basin. *Mar Pet Geol.* 2018;92:842–54. <https://doi.org/10.1016/j.marpetgeo.2017.12.018>.
- Wang L, Zhao N, Sima L, Meng F, Guo Y. Pore structure characterization of the tight reservoir: systematic integration of mercury injection and nuclear magnetic resonance. *Energy Fuels.* 2018a;32:7471–84. <https://doi.org/10.1021/acs.energyfuels.8b01369>.
- Wang RF, Chi YG, Zhang L, He R, Tang Z, Liu Z. Comparative studies of microscopic pore throat characteristics of unconventional super-low permeability sandstone reservoirs: examples of Chang 6 and Chang 8 reservoirs of Yanchang Formation in Ordos Basin, China. *J Pet Sci Eng.* 2018b;160:72–90. <https://doi.org/10.1016/j.petrol.2017.10.030>.
- Wu H, Ji YL, Liu RE, Zhang C, Chen S. Insight into the pore structure of tight gas sandstones: a case study in the Ordos Basin, NW China. *Energy Fuels.* 2017;31:13159–78. <https://doi.org/10.1021/acs.energyfuels.7b01816>.

- Xi KL, Cao YC, Haile BG, Zhu R, Jahren J, Bjørlykke K, et al. How does the pore-throat size control the reservoir quality and oiliness of tight sandstones? The case of the Lower Cretaceous Quantou Formation in the southern Songliao Basin, China. *Mar Pet Geol.* 2016;76:1–15. <https://doi.org/10.1016/j.marpetgeo.2016.05.001>.
- Xiao DS, Jiang S, Thul D, Lu S, Zhang L, Li B. Impacts of clay on pore structure, storage and percolation of tight sandstones from the Songliao Basin, China: implications for genetic classification of tight sandstone reservoirs. *Fuel.* 2018;211:390–404. <https://doi.org/10.1016/j.fuel.2017.09.084>.
- Xie RH, Xiao LZ. Advanced fluid-typing methods for NMR logging. *Pet Sci.* 2011;8(2):163–9. <https://doi.org/10.1007/s12182-011-0130-4>.
- Yang H, Fu JH, Liu XS, Meng P. Accumulation conditions and exploration and development of tight gas in the Upper Paleozoic of the Ordos Basin. *Pet Explor Dev.* 2012;39(3):315–24. [https://doi.org/10.1016/S1876-3804\(12\)60047-0](https://doi.org/10.1016/S1876-3804(12)60047-0).
- Yang RC, Fan AP, Van Loon AJ, Han Z, Wang X. Depositional and diagenetic controls on sandstone reservoirs with low porosity and low permeability in the Eastern Sulige Gas Field, China. *Acta Geol Sin (Engl Ed).* 2014;88(5):1513–34. <https://doi.org/10.1111/1755-6724.12315>.
- Yang Z, He S, Guo XW, Li Q, Chen Z, Zhao Y. Formation of low permeability reservoirs and gas accumulation process in the Daniudi Gas Field, Northeast Ordos Basin, China. *Mar Pet Geol.* 2016;70(17):222–36. <https://doi.org/10.1016/j.marpetgeo.2015.10.021>.
- Yang Z, Li QY, Wu ST, Lin S, Liu X. Evidence of the near-source accumulation of the tight sandstone gas in northern Ordos Basin, north-central China. *Acta Geol Sin (Engl Ed).* 2017;91(5):1820–35. <https://doi.org/10.1111/1755-6724.13413>.
- Zeng LB, Wang ZG, Zhang GB. A comprehensive evaluation method for low-permeability reservoirs. *Pet Sci.* 2005;2(4):9–13.
- Zeng JH, Cheng SW, Kong X, Guo K, Wang H. Non-Darcy flow in oil accumulation (oil displacing water) and relative permeability and oil saturation characteristics of low-permeability sandstones. *Pet Sci.* 2010;7(1):20–30. <https://doi.org/10.1007/s12182-010-0003-2>.
- Zhang YG. Study on micro geological feature of tight sandstone gas reservoir at eastern part of Sulige gas field, Ordos Basin. Master thesis. 2014. Northwest University, China (in Chinese).
- Zhang LC, Lu SF, Xiao DS, Li B. Pore structure characteristics of tight sandstones in the northern Songliao Basin, China. *Mar Pet Geol.* 2017;88:170–80. <https://doi.org/10.1016/j.marpetgeo.2017.08.005>.
- Zhang SM, Cao YC, Jahren J, Zhu R, Mao Z, Xi K, et al. Pore characteristics of the fine-grained tight reservoirs in the Yabulai Basin, northwestern China. *Acta Geol Sin (Engl Ed).* 2018;92(3):1170–92. <https://doi.org/10.1111/1755-6724.13598>.
- Zhao CL, Hu AM, Chen BY, et al. The oil and gas industry standard of the People's Republic of China, the oil and gas reservoir evaluation methods. Beijing: Petroleum Industry Press; 1998. p. 16 (in Chinese).
- Zhao HW, Ning ZF, Wang Q, Zhang R, Zhao T, Niu T, et al. Petrophysical characterization of tight oil reservoirs using pressure-controlled porosimetry combined with rate-controlled porosimetry. *Fuel.* 2015;154:233–42. <https://doi.org/10.1016/j.fuel.2015.03.085>.
- Zou CN, Gong YJ, Tao SZ, Liu S. Geological characteristics and accumulation mechanisms of the “continuous” tight gas reservoirs of the Xu2 Member in the middle-south transition region, Sichuan Basin, China. *Pet Sci.* 2013a;10(2):171–82. <https://doi.org/10.1007/s12182-013-0264-7>.
- Zou CN, Yang Z, Tao SZ, Yuan XJ, Zhu RK, Hou LH, et al. Continuous hydrocarbon accumulation over a large area as a distinguishing characteristic of unconventional petroleum: the Ordos Basin, North-Central China. *Earth Sci Rev.* 2013b;126(9):358–69. <https://doi.org/10.1016/j.earscirev.2013.08.006>.
- Zou CN, Zhai GM, Zhang GY, Wang H, Zhang G, Li J, et al. Formation, distribution, potential and prediction of global conventional and unconventional hydrocarbon resources. *Pet Explor Dev.* 2015a;42(1):13–25. [https://doi.org/10.1016/s1876-3804\(15\)60002-7](https://doi.org/10.1016/s1876-3804(15)60002-7) (in Chinese).
- Zou CN, Yang Z, Zhu RK, Zhang G, Hou L, Wu S, et al. Progress in China's Unconventional oil and gas exploration and development and theoretical technologies. *Acta Geol Sin (Engl Ed).* 2015b;89(3):938–71. <https://doi.org/10.1111/1755-6724.12491>.